Systematic Operating Temperature Differences Between Al-BSF, PERC, and PERT-With-Optimized-Rear-Reflector Solar Mini-Modules Due to Rear Reflectance

Jonathan L. Bryan, Timothy J. Silverman, Michael G. Deceglie, Mason Mahaffey, Peter Firth, and Zachary C. Holman

***Abstract*—Reflecting sub-bandgap light from photovoltaic modules has the potential to improve lifetime energy generation of fielded systems by reducing operating temperature. In this article, the temperature of fielded aluminum back-surface field (Al-BSF) and passivated emitter and rear contact (PERC) mini-modules was monitored every 5 minutes for 75 days along with corresponding meteorological data. Additionally, passivated emitter rear totally diffused (PERT) mini-modules with high-performance sub-bandgap rear reflectors were tested and compared to the state-of-the-art industrial modules. These reflectors consisted of a >300-nm-thick silicon dioxide nanoparticle film with a low refractive index. The impact of reflectance on measured operating temperature was isolated with a previously developed thermal model and quantified as the reflectance-induced median temperature difference between each tested module at representative outdoor conditions (1000 W·m^{-2}, 25 °C ambient temperature, and 1.43 m·s^{-1} wind speed). We found that, because of their reflectance differences, PERC modules ran systematically cooler than Al-BSF modules by 1.0 °C, whereas the PERT-with-optimized-rear-reflector systematically operated 1.4 °C cooler than the Al-BSF module and 0.4 °C than the PERC module. We also found that the rear reflector provided the greatest temperature benefit during periods of highest irradiance.**

***Index Terms*—Optics, photovoltaic cells, photovoltaic systems, solar panels, thermal management.**

Manuscript received August 26, 2021; revised October 26, 2021; accepted November 8, 2021. This work was supported in part by the National Renewable Energy Laboratory, operated by Alliance for Sustainable Energy, LLC, for the U.S. Department of Energy under Contract DE-AC36-08GO28308 and in part by the U.S. Department of Energy Office of Energy Efficiency and Renewable Energy Solar Energy Technologies Office under Agreement 30312. *(Corresponding author: Jonathan L. Bryan.)*

Jonathan L. Bryan and Mason Mahaffey are with the School of Electrical Computer and Energy Engineering, Arizona State University, Tempe, AZ 85287 USA (e-mail: jlbryan5@asu.edu; mpmahaff@asu.edu).

Timothy J. Silverman and Michael G. Deceglie are with the National Renewable Energy Laboratory, Golden, CO 80401 USA (e-mail: timothy.silverman@nrel.gov; michael.deceglie@nrel.gov).

Peter Firth and Zachary C. Holman are with the School of Electrical Computer and Energy Engineering, Arizona State University, Tempe, AZ 85287 USA, and also with Swift Coat Inc., Tempe, AZ 85284 USA (e-mail: peter@swiftcoat.com).

Color versions of one or more figures in this article are available at https://doi.org/10.1109/JPHOTOV.2021.3127447.

Digital Object Identifier 10.1109/JPHOTOV.2021.3127447

I. Introduction

PHOTOVOLTAIC (PV) cells are typically characterized at standard test conditions (STC) of 25 °C and AM1.5G irradiance. When installed in the field, however, cells are encapsulated in module materials and operate at meteorological and irradiance conditions different than STC [1], [2]. This leads to operating temperatures higher than 25 °C, and even exceeding 70 °C in some cases [3], [4]. The waste heat generated in the module has a large impact on the energy yield of an outdoor system. The power output of the module decreases as its operating temperature increases; this loss is commonly described by a temperature coefficient [5]. For commercial silicon PV technology, the temperature coefficient of efficiency ranges from approximately −0.38%/°C for high-quality monocrystalline passivated emitter rear totally diffused (PERT) to −0.4%/°C for passivated emitter and rear contact (PERC) modules to −0.43%/°C for traditional aluminum back-surface field modules (Al-BSF) [6]. Higher module temperature not only reduces instantaneous operating efficiency but also accelerates nearly every type of module degradation [7]. For instance, rates of encapsulant browning were higher during accelerated testing of field-aged silicon modules when they were held at 85 °C compared to 60 °C; this resulted in a relative short-circuit current (I_{sc}) drop of 3.26% for the warmer module and 1.37% for the cooler one [8]. Thus, reducing operating temperature in the field results in higher power conversion efficiency and longer system lifetime, manifesting as lower levelized cost of electricity and greater value for the end user [9]. As a result, a broad range of thermal mitigation strategies has been investigated [10].

The waste heat in the module originates from two sources: losses in the process of converting radiative energy to electrical energy (thermalization, nonradiative recombination, transport, Carnot, etc.) and parasitic absorption of light in the module that does not lead to electrical energy generation [11]. The former are fundamental limitations in the PV energy conversion process and minimizing their degree through efficiency enhancement has long been the focus of PV research; the single-junction silicon efficiency record is currently 26.7%, just short of the approximate 29% intrinsic limit [12]. A particularly insidious form of the latter heating mechanism is the parasitic absorption of light that does not contain sufficient energy to create electron–hole pairs in the absorber, known as sub-bandgap radiation. In the case of silicon, with a bandgap of 1.12 eV, approximately 19% of incident solar radiation is sub-bandgap [13]. Thermal modifications focusing on sub-bandgap radiation present a particularly attractive opportunity to reduce PV module operating temperature since the source of heat is both large and fundamentally avoidable in the energy conversion process. Indeed, multiple studies have found increasing sub-bandgap reflection to be among the most worthwhile thermal management approaches [14]–[16].

The ideal implementation of this thermal management strategy would result in 100% reflectance of sub-bandgap light. Silverman *et al.* [14] modeled this idealized structure and calculated a 3.8 °C difference in annual irradiance-weighted temperature between a standard Al-BSF module and one with such an ideal sub-bandgap reflector. For a module with a temperature coefficient of −0.4%/ °C, a 3.8 °C temperature decrease results in a 1.52% absolute gain in efficiency. In Silverman's work, the ideal sub-bandgap reflector operated on the front side of the module. Slauch *et al.* [17] further developed this approach to show how reflector designs at the front air/glass interface can impact thermal and energy benefits in real-world conditions. In simulations, a 13-layer sub-bandgap mirror and 20-layer mirror on the outer air/glass interface increased reflectance at the peak sub-bandgap wavelength by 52% and 73%, respectively, and reduced parasitic absorption in the silicon module by 41 and 51 $W \cdot m^{-2}$, respectively. Each of these mirror designs increased calculated annual energy yield by at least 3.6% compared to a baseline module through a combination of higher transmittance of super-bandgap light (optical benefit) and higher reflectance of sub-bandgap light (thermal benefit) [18]. These energy benefit calculations are before accounting for accelerated module degradation associated with higher operating temperature of modules without optimized sub-bandgap reflectors.

Double-layer stacks provide an easier and less expensive route to implementation; simulated double-layer stacks of MgF_2/Al_2O_3 produced approximately 0.8% annual energy yield increase relative to standard module glass anti-reflection coatings [19]. While front-side reflectors can minimize parasitic absorption in the front module materials, a drawback of front-side reflectors is the additional constraint of effective transmission of light above the bandgap and a requirement for durable materials that can maintain their properties while exposed to the ambient for decades. More recent calculations by Slauch *et al.* [20] found that an optimized reflector at the interface between the front encapsulant and the cell reduces annual power-weighted average operating temperature under realistic power-generating conditions by up to 2.2 °C for Al-BSF modules and 1.8 °C for PERC modules, respectively.

An alternative location for a sub-bandgap reflector is the rear side of the solar cell. Inserting dielectric/metal stacks on the rear side of a silicon wafer can drastically increase reflectance. For instance, $SiN_x/Si/MgF_2/Ag$ test structures exhibited sub-bandgap reflectance over 90% and average per-bounce internal reflectance greater than 99.5% [21]. With these structures, Holman *et al.* showed that parasitic absorption in the metal is primarily caused by the evanescent field of high-incidence-angle p-polarized light reaching the metal surface, thereby exciting surface plasmon polaritons [22]. The thickness and the refractive index of the dielectric interlayer strongly affect the penetration depth of the electric field, and they can thereby be tuned to maximize reflectance. Further studies investigating the influence of surface texturing, dielectric refractive index, and metal composition have yielded some general design rules to optimize rear reflectance: the dielectric thickness should be at least 200 nm and its refractive index should be as low as possible [23]. While engineering the sub-bandgap reflector to be on the rear side leaves the cell prone to parasitic absorption by the layers at the front of the module and cell, it nonetheless has significant potential for module temperature reduction because of the outsized role that the rear metal plays. Slauch *et al.* [20] found that increasing internal reflection at the rear surface of an Al-BSF cell from 67% to 100% can provide up to 1.2 °C annual average temperature decrease and up to 2.8 °C cooling under one-sun conditions.

Metal electrodes directly on the rear of silicon wafers—particularly those formed from pastes—can absorb the majority of longer wavelength light that does not get absorbed in the wafer, as exhibited in Al-BSF cells. High-temperature firing of the printed Al paste forms Al+Si interface regions between the silicon wafer and pure Al electrode due to interdiffusion and alloying of Al and Si [24]. Optical modeling of silicon modules by Subedi *et al.* [24] showed over a 20% difference absolute in reflectance at 1200 nm between Si/Al structures with and without the Al+Si interfacial region. The same highly absorptive Al+Si region also exists in PERC devices, though minimizing its volume is the core design principle behind PERC. In addition to the total contacted area, the 3-D geometry of the cell's contact region affects sub-bandgap optics, as the Al+Si region diffuses vertically from the contact opening into the Si wafer and also laterally into the absorber regions adjacent to the contact openings. Detailed models have recently been developed to simulate reflectance for Al-BSF cells and PERC cells with contact geometries consisting of lines or dashes. These results showed reflectances, R, at 1200 nm of 15.9%, 23.1%, and 28.1%, respectively, highlighting the optical benefit of the rear dielectric passivation stack of PERC [25].

As emphasized previously, this optical benefit can translate to a thermal benefit. Under computer-simulated AM1.5G irradiation, Vogt *et al.* showed that modeled PERC structures operated 1.7 °C cooler than Al-BSF, 0.8 °C of which was due to higher efficiency (1.9% absolute in this study), and 0.9 °C of which was attributable to lower parasitic absorption in the rear metal electrode [26]. The reflected portion of the AM1.5G spectrum was 126.3 and 143.2 $W \cdot m^{-2}$ for Al-BSF and PERC, respectively. Though there is evidence to suggest the superior sub-bandgap reflectance of PERC would yield a temperature benefit in real outdoor operating conditions, this has not yet been demonstrated, to the authors' knowledge. Tests on fielded modules are an important step to validate thermal benefits of new materials and predict consequential energy production benefits, as spectral and angle-of-incidence variation affect module optics [3], [18]. Furthermore, while the dielectric passivation in the PERC cell has an appreciable impact on reflectance, and consequently on temperature, the reflectance is still far from the possible reflectance of 90% demonstrated by Holman *et al.* [21]. Thus, there is a large opportunity to lower module operating temperature by implementing ideal rear dielectric layers into industrially manufactured silicon PV cells.

In this article, we test this thermal management approach by including an optimized sub-bandgap reflector in PERT solar cells. These cells are fabricated into mini-modules that are deployed outdoors for testing. The dielectric layer introduced is a porous SiO_2 nanoparticle (NP) coating with optimized thickness and low refractive index, which yields a higher sub-bandgap reflectance than even PERC cells [27]. Also included in the outdoor tests are mini-modules with commercial Al-BSF and PERC cells. The three modules were exposed over 75 days to a wide range of irradiance and ambient conditions, representative of real, energy-generating environments. The module performance and meteorological conditions were measured throughout the test period and used as inputs in a previously developed thermal model to calculate systematic differences in thermal behavior attributable exclusively to differences in module reflectance [28].

II. Methods

A. Module Fabrication, Characterization, and Outdoor Installation

This test used M2-sized (156.75 × 156.75 mm) Al-BSF, PERC, and modified n-PERT solar cells. Schematics of each of these cells are shown in Fig. 1. The Al-BSF cells were obtained from a commercial vendor; the PERC and PERT (BiSoN) cells were from ISC Konstanz. No modifications were performed on the Al-BSF and PERC cells before incorporating them into modules.

The as-received bifacial PERT cells, however, were augmented with a dielectric/Ag reflector stack on the rear side, thereby converting the cells into monofacial and allowing a straightforward comparison to the (also monofacial) Al-BSF and PERC. Here, silicon dioxide (SiO_2) NP films with a porosity of approximately 55%—corresponding to a refractive index of 1.2—an average pore size below 10 nm, and a thickness of at least 300 nm were deposited on the rear side of the PERT cells via aerosol impact-driven assembly [29]. Silicon- and oxygen-containing precursors were used to synthesize stoichiometric SiO_2 NPs with average particle size of approximately 5 nm, which were accelerated from the synthesis chamber to the substrate by a controlled pressure gradient. This method has previously been used to deposit low-refractive-index porous Si NPs as a rear reflector layer for silicon heterojunction cells [30]. The SiO_2 NP synthesis process used here enables lower refractive index films than our previously studied Si NPs. Further descriptions of the deposition and film characterization processes can be found in prior work [27].

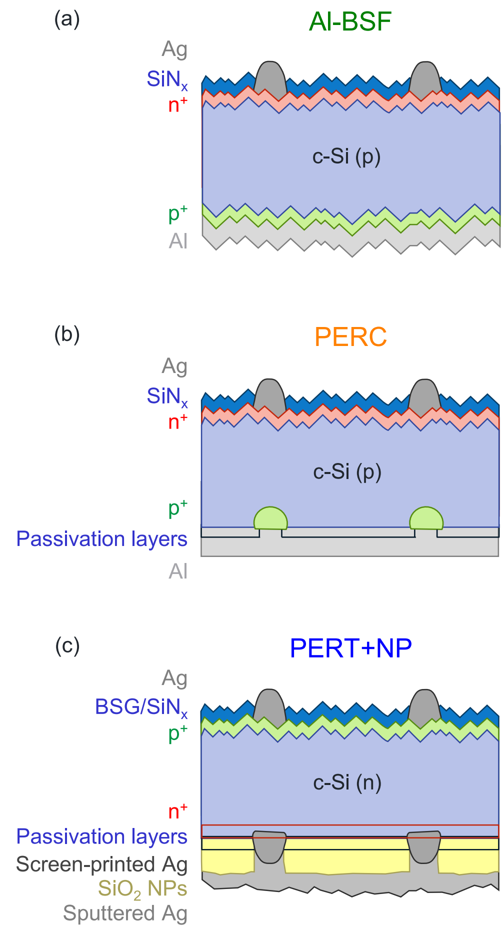

Fig. 1. Schematics of (a) Al-BSF, (b) PERC, and (c) PERT+NP cells used in the mini-modules in this article.

During the deposition of the SiO_2 NPs on the rear of the PERT cells, the silver busbars were covered with a shadow mask to maintain the electrical contact already established by the rear-side screen-printed Ag grid. Sputtered Ag layers were then deposited on the full area of the rear side, per Fig. 1(c), using an MRC 944 tool with a dc source power of 1 kW. Hereafter, we call these cells "PERT+NP." This processing sequence is not industrially compatible, but was the most expedient and practical approach for the demonstration sought here, as prior tests integrating the porous SiO_2 NP film directly into an established PERC fabrication sequence yielded no optical benefit due to the fire-through paste reacting with the NP film [27].

Another set of PERT cells were converted into monofacial but did not include the SiO_2 NP film. Instead, Al was sputtered on the full area of these as-received cells to serve as optical references. These cells, referred to as "PERT no NP reference," were not converted into modules. External quantum efficiency (EQE) and reflectance spectra of each set of cells were measured from 300 to 2500 nm using a PV Measurements QEX10 tool and a PerkinElmer Lambda 950 spectrophotometer. These measurements were used to find active-area, AM1.5G-weighted

R for each cell. After cell characterization, the Al-BSF, PERC, and PERT+NP cell batches were packaged into modules.

Each module contained nine M2-sized cells. The cells were electrically connected in series and arranged in a closely spaced 3×3 grid. The cells were packaged with conventional PV module materials: textured low-iron cover glass (no antireflection coating), ethyl vinyl acetate (EVA) encapsulant, and a polyvinyl fluoride (PVF)/polyethylene terephthalate/PVF backsheet. Each module used a pair of small, single-pole junction boxes, placed entirely in the margin area away from the cells. Electroluminescence imaging after module packaging was performed to ensure that interconnection and lamination had been completed without major damage to the cells. The Al-BSF, PERC, and PERT+NP modules had STC aperture efficiency values of 17.7%, 18.3%, and 18.5%, respectively. Module reflectance and EQE were measured using a Lambda 1050 and NREL's filter EQE system described in prior work [31].

We deployed the modules at NREL's outdoor test facility in Golden, Colorado for 75 days. They were oriented to the south at 40° tilt above horizontal. Current–voltage (*I–V*) curves were collected every 5 minutes and the modules were held at their maximum power points between measurements. In addition to *I–V* data, simultaneous measurements of ambient temperature (T_{ambient}), wind speed (v_w), and plane-of-array irradiance (E_{POA}) were also collected.

Module temperature (T_{module}) was derived from the *I–V* bilinear interpolation method [32]. Indoor pulse *I–V* sweeps of each module were performed at each combination of device temperature (15, 20, 25, 30, 35, 40, 45, 50, 55, and 60 °C) and irradiance (200, 400, 600, 800, and 1000 $\mathrm{W{\cdot}m^{-2}}$). Sixteen thermistors were placed on the back of each module for temperature measurement. Module temperature was uniform to within ±2.25 °C. Once thermal uniformity was established, the *I–V* curve was recorded and associated with single-point temperature measurement in the center of the module, made with a resistance temperature detector. The open-circuit voltage (V_{oc}) and I_{sc} from the outdoor *I–V* sweeps were plugged into an interpolation grid containing 50 grid points from the temperature-controlled, indoor *I–V* sweeps, to extract T_{module}. This method has been shown to have good accuracy for measuring module temperature [33]. Systematic errors are assumed to affect each of the module types in the same way and are thus neglected to compare relative operating temperatures outdoors.

B. Outdoor Data Analysis

To assess differences in temperature caused by the differences in sub-bandgap reflectance between each module, a correction factor is applied to the measured data. This correction procedure eliminates temperature variation arising from the other major contributors of temperature variation: irradiance, wind, and module efficiency. The correction factor f is defined as

$$\begin{aligned} f &= f_{\mathrm{irradiance}} \times f_{\mathrm{wind}} \times f_{\mathrm{efficiency}} \\ &= \frac{E_{\mathrm{POA}}^{(\mathrm{ref})}}{E_{\mathrm{POA}}^{(\mathrm{meas})}} \times \frac{c(v_w^{(\mathrm{ref})})}{c(v_w^{(\mathrm{meas})})} \times \frac{1-\eta_{\mathrm{STC}}^{(\mathrm{ref})}}{1-\eta_{\mathrm{STC}}^{(\mathrm{meas})}} \end{aligned} \quad (1)$$

TABLE I

CORRECTION FACTOR VARIABLES AND REFERENCE VALUES

Symbol	Quantity	Reference value
$\boldsymbol{E}_{\mathbf{POA}}$	plane-of-array irradiance	1000 $\mathrm{W{\cdot}m^{-2}}$
$\boldsymbol{v_w}$	wind speed	1.43 $\mathrm{m{\cdot}s^{-1}}$
$\boldsymbol{c(v_w)}$	lumped heat transfer factor	0.0256
$\boldsymbol{\eta}_{\mathbf{STC}}$	STC efficiency	17.7%

where E_{POA} is plane-of-array irradiance, $c(v_w)$ is the wind-dependent heat-transfer factor, and η_{STC} is STC efficiency. The lumped heat-transfer factor used here is an empirically derived function of wind speed, the dominant heat transfer mechanism in fielded modules [34]. Its derivation method is detailed in prior work [35]. The full derivation of the correction term f is also described in detail in prior work [28]. Measured values are represented with superscript (meas) and reference values with superscript (ref). The reference ambient conditions and reference module properties used in this experiment are shown in Table I. These values were chosen to minimize the average magnitude of the correction and to be representative of the most relevant energy-generating conditions.

The raw temperature rise above ambient ΔT^{raw} is

$$\Delta T^{\mathrm{raw}} = T_{\mathrm{module}}^{(\mathrm{meas})} - T_{\mathrm{ambient}}^{(\mathrm{meas})}. \quad (2)$$

The correction factor based on the reference values is applied to the measured values for each module to calculate the corrected temperature rise above ambient ΔT as follows:

$$\Delta T = \Delta T^{\mathrm{raw}} \times f. \quad (3)$$

The corrected temperature rise ΔT represents what the module temperature rise above ambient *would have been* if the module under test had the reference properties and had been measured under the reference conditions [28]. As the correction factor eliminates temperature differences from other major factors, differences in ΔT between modules are caused exclusively by differences in reflectance. That is, two modules with the same reflectance will have the same ΔT, even if they have different efficiencies or were measured with different irradiances and wind speeds. The ΔT values of each module throughout the 75-day test period are used to facilitate comparisons between the modules, which have different reflectances.

To minimize deviation from the steady-state energy balance between the module under test and the ambient—the basis of the thermal model—data were removed at instances with appreciable snow, large changes in irradiance, or large changes in wind speed. For irradiance, the data were removed if the difference between the maximum and minimum measured values was greater than 3 $\mathrm{W{\cdot}m^{-2}}$ for 30 s before and after the measurement. For wind speed, the data were filtered if the difference between the maximum and minimum measured values was greater than 5 $\mathrm{m{\cdot}s^{-1}}$ for the 12 minutes before the measurement. The presence of snow was detected by comparing the predicted I_{sc} of the module to the measured I_{sc}. The predicted I_{sc} is defined as the median I_{sc} between 950–1050 $\mathrm{W{\cdot}m^{-2}}$ multiplied by the quantity (measured I_{sc} / 1000 W·m^{-2}). The data were removed if the ratio of the measured I_{sc} to the predicted I_{sc} was not between 0.85 and 1.15.

III. Results and Discussion

A. Sample Characterization

The reflectance of the cells before module packaging is shown in Fig. 2(a). As the front Ag fingers of the completed cells fell within the aperture of the reflectance measurements, the reflectance data were corrected to represent active-area reflectance by dividing by the unmetallized areal fraction. The reflectance at 1200 nm approaches 55% for the PERT+NP cells—the best ever demonstrated for a PERT or PERC cell, to the authors' knowledge. The PERT+NP had higher reflectance than the PERT reference with full-area Al metallization, revealing the effectiveness of the SiO_2 NP film/Ag rear reflector stack. Additionally, the PERT+NP reflectance was higher than by the Al-BSF and PERC cells. The reason the PERT+NP cells do not reach the over 90% reflectance seen in prior work is infrared parasitic absorption occurring in heavily doped regions besides the rear reflector.

EQE and $1-R$ for the fully fabricated modules are shown in Fig. 2(b), with AM1.5G-weighted R values shown in parentheses. The module materials impart parasitic absorption and reduce the reflectance benefit of the rear reflector. R at 1200 nm for the PERT+NP cell was 54.5% and dropped by 17.3% absolute to 37.2% after module packaging. For PERC and Al-BSF, this drop after module packaging was 12.1% and 2.1%, respectively. The reduction in R is attributable to parasitic absorption by the glass and to a larger degree by the EVA, which has several characteristic absorption peaks visible in Fig. 2(b). Similarly, Vogt *et al.* [26] calculated 38.0 W·m^{-2} and 43.7 W·m^{-2} of parasitic absorption in the glass and EVA layers for Al-BSF and PERC modules, respectively, in the 1210–2500 nm spectral range. Haedrich *et al.* calculated the annual energy loss of a PERC module to be 4.4% due to module embedding, primarily from front cover glass reflectance and also parasitic absorption in the module glass and EVA [3]. Higher reflectance also contributes to improved EQE in the 1000–1200 nm wavelength range because this light gets a longer path length through the silicon.

The impact of parasitic absorption by the module materials in the super- and sub-bandgap ranges for the devices tested here can be seen in Fig. 2(c). Super-bandgap (250–1100 nm) reflectance is undesirable. While it does reduce module operating temperature, it also reduces I_{sc} and should thus be avoided. The most desirable outcome is to minimize the purple bars and maximize the red bars (though the red bars will not exceed 19%). The AM1.5G-weighted reflectance for the PERT+NP module was 11.2%, 6.3% of which was in the 250–1100 nm range. This reveals that, of the approximately 19% sub-bandgap light, the PERT+NP module rejected just 4.9%, even though optimized test structures demonstrated a path to 90% reflectance at 1200 nm. The difference in sub-bandgap AM1.5G-weighted R (red bars) between cell and module for Al-BSF, PERC, and PERT+NP is 0.93, 2.59, and 3.14% absolute, respectively. This shows that the superior sub-bandgap reflectance of the PERT+NP cell does not entirely carry over after module packaging, revealing that improvements in sub-bandgap reflectance at the rear side must be in coordination with the optical properties of the fully fabricated module to capture the full thermal benefit.

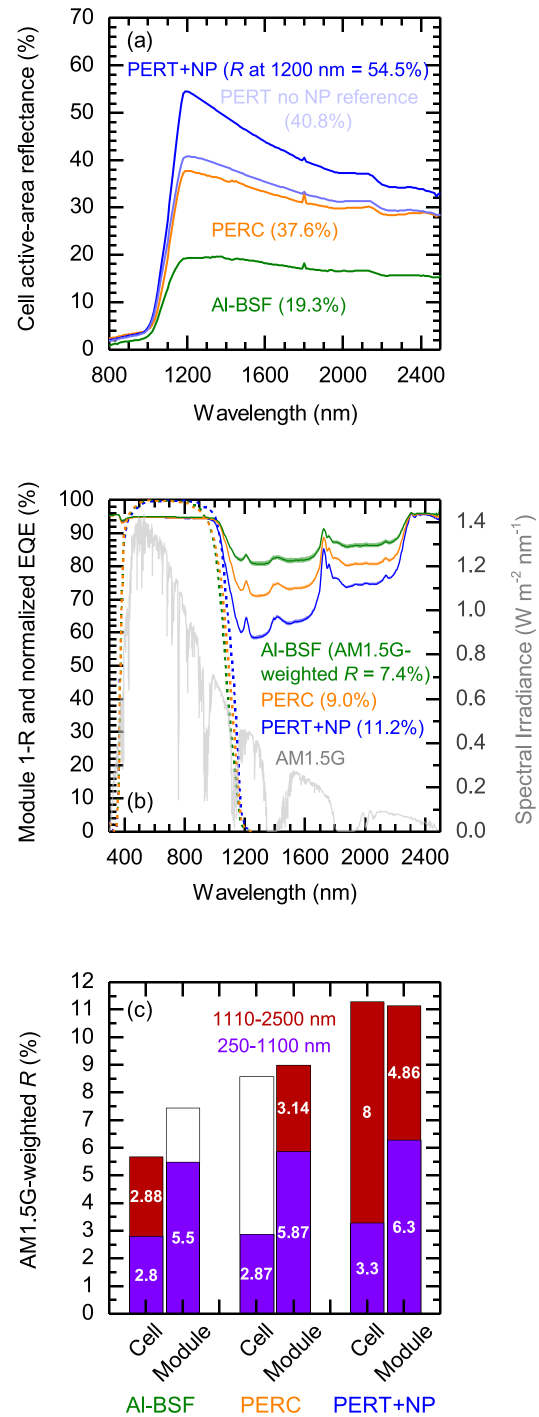

Fig. 2. Plot of (a) active-area R for each cell, (b) $1-R$ and normalized EQE for the fully fabricated modules, and (c) AM1.5G-weighted R for each cell and module. The full height is the reflection from 250–2500 nm, with sub-bands as indicated.

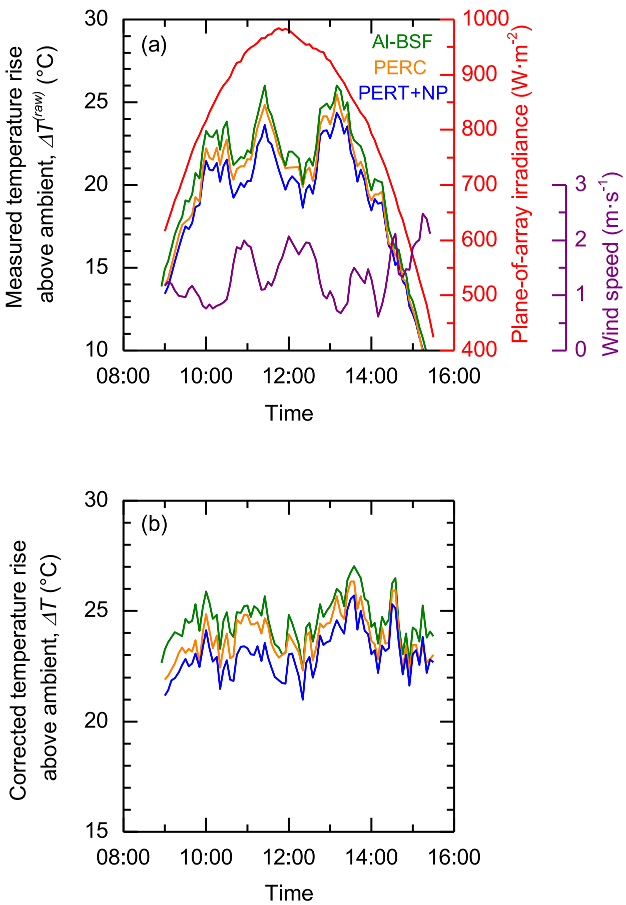

Fig. 3. (a) Measured module temperature rise above ambient and irradiance for one day in the test period (December 9th). (b) Corrected module temperature rise above ambient from the same day.

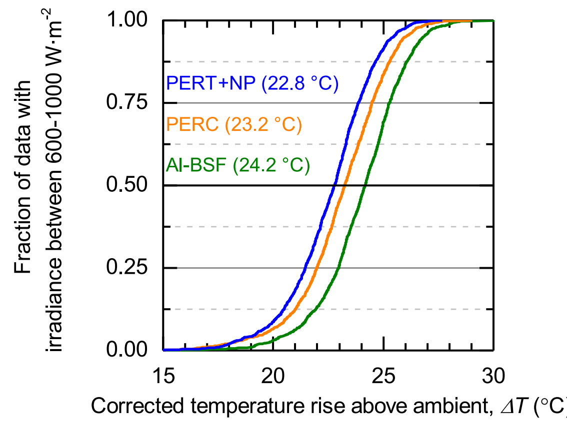

Fig. 4. Corrected temperature rise above ambient for each tested module displayed as a cumulative distribution function (CDF). The median values for each tested module are shown in parentheses.

B. Outdoor Data

Fig. 3(a) shows ΔT^{raw} with corresponding irradiance and wind speed data from one day in the test range where nearly all data met the steady-state energy balance requirements. Since each set of module data is from the same moment, the differences between ΔT^{raw} values are not due to meteorological factors, but rather only from the differences in module performance (efficiency and reflectance). Systematic temperature differences on this day are revealed by the raw data: PERT+NP runs cooler than PERC, which in turn runs cooler than Al-BSF. As expected, in a given day with large irradiance changes, relatively large changes in module operating temperature are also observed. Note that the module temperature does not follow the irradiance precisely because of the variable wind speed: the approximately 1 m·s^{-1} increases in wind speed at 10:30 and 12:00 reduce the temperature by several degrees. Fig. 3(b) shows the corresponding ΔT for this same day, which collapses the data around a tighter distribution of temperature values. As a reminder, ΔT are the module temperature rise above ambient that the modules would have experienced if they all shared the performance characteristics and measurement conditions in Table I. The corrected data similarly show a systematic difference in ΔT between modules, which in this corrected case, is due just to reflectance as the correction accounts for differences in efficiency.

Fig. 4 plots ΔT for each module, in the 600–1000 W·m^{-2} irradiance range, as a cumulative distribution function (CDF). The median ΔT value occurs when the CDF equals 0.5; each module operates warmer than its median value for half of the time and cooler than this value for the other half of the time. For the Al-BSF, PERC, and PERT+NP modules, the median ΔT value was 24.2, 23.2, and 22.8 °C, respectively. The difference between these median values is a good metric into which all of the data can be consolidated to yield a single temperature benefit value attributable to reflectance. At the chosen reference conditions (1000 W·m^{-2}, 1.43 m·s^{-1}, and 25 °C), the PERC module operates 1.0 °C cooler than Al-BSF, and the PERT+NP module operates 1.4 °C cooler than Al-BSF and 0.4 °C cooler than PERC. For a module with a temperature coefficient of −0.4 %/°C, 1.4, and 0.4 °C temperature decreases result in 0.56 and 0.16% absolute gains in efficiency, respectively. The statistical significance of these median differences is validated with Mann–Whitney U tests: the medians are statistically different at over a 0.01 level (Z scores of 7.9, 12.7, and 20.2, respectively). Thus, there is a clear and systematic difference in operating temperature attributable to the sub-bandgap reflectance of each module. The 1.0 °C temperature benefit of PERC relative to BSF from reflectance measured here is consistent with the 0.9 °C calculated by Vogt *et al.* [26] for the same 1000 W·m^{-2} irradiance.

In evaluating the relative thermal performance of one cell design against others, it is instructive to compare the temperatures of pairs of modules. Fig. 5 shows differences between module temperatures taken at the same time and corrected just for efficiency, making the temperature differences due solely to reflectance. The data are binned according to irradiance and the total plotted range of 600–1000 W·m^{-2} accounts for approximately 86% of the power production for the Al-BSF module in this article. The mean temperature benefit of the PERT+NP module over the Al-BSF and PERC modules increases at higher irradiance, revealing that this thermal management approach has

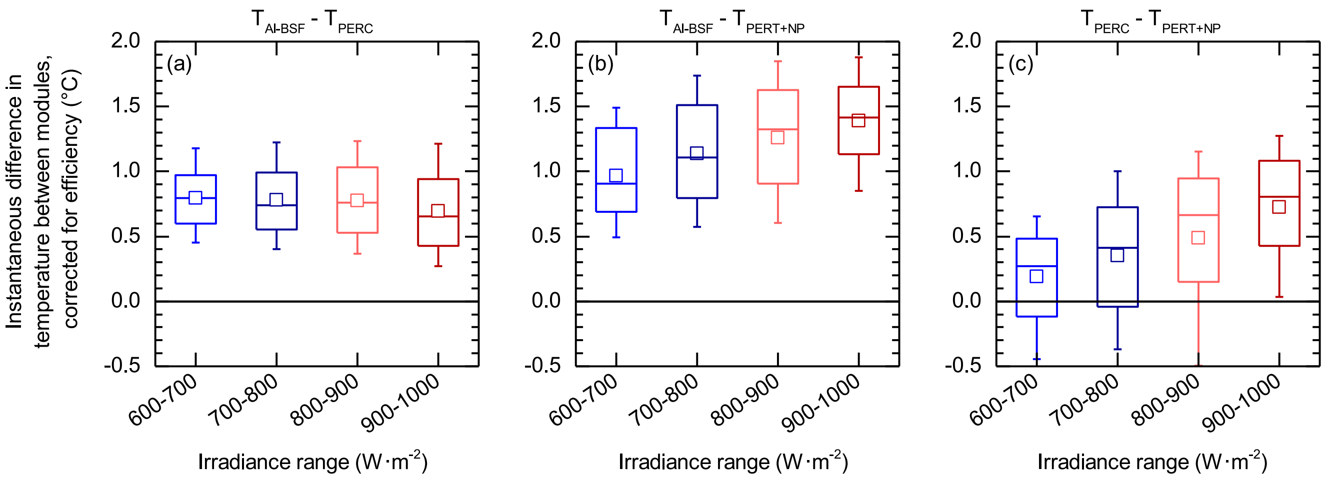

Fig. 5. Temperature difference between (a) Al-BSF and PERC, (b) Al-BSF and PERT+NP, and (c) PERC and PERT+NP modules displayed as boxes and whiskers and binned by irradiance. Boxes represent 25–75 percentiles, whiskers represent 10–90 percentiles, and inset boxes and lines represent mean and median values, respectively.

the largest impact at the most important conditions: high irradiance and, consequently, high power generation. The Al-BSF and PERC comparison, surprisingly, does not show this same irradiance dependence. We hypothesize that this may be due to noise from the indoor interpolation method related to spectral mismatch between the Xenon flash lamp and typical outdoor irradiance.

IV. Conclusion

Fielded modules can benefit from the thermal management strategy of rejecting unusable sub-bandgap light, thereby improving lifetime energy production. Here, we found that adding an optimized rear-reflector stack provides a temperature benefit of 1.4 and 0.4 °C over fielded Al-BSF and PERC modules, respectively. Importantly, we found that the rear SiO_2 NP/Ag reflector is most effective during periods of highest irradiance, when power generation is highest. To capture the full temperature benefit of approximately 2.8 °C associated with this approach, parasitically absorbing materials such as module glass and EVA should be replaced with low-infrared-absorbing alternatives, and heavily-doped regions in the cell should be strategically localized.

The technique used here to implement the reflector technology—converting a bifacial cell to monofacial—is not suitable for industrial application. In a previous study, we found the porous SiO_2 film to be chemically incompatible with the etching mechanism of fire-through Al pastes. However, this limitation is not insurmountable. Just as traditional Al-BSF paste chemistries were modified to prevent damage to the SiN_x passivation layers in PERC cells, additional paste optimization could enable an optimized optical film that complements the dielectric passivation stack [36]. Similarly, making pastes less damaging is an active area of research for polysilicon contacts [37]. Integrating low-refractive-index dielectric layers with more gentle paste chemistries could be a worthwhile cell development effort, especially in cases where bifaciality is irrelevant and thermal management via sub-bandgap reflectance is particularly important. Such cases include residential and commercial rooftop systems, where conductive/convective cooling of modules is reduced or completely suppressed and higher module temperatures create higher building cooling loads in summer [15]. Furthermore, such dedicated optical films can be integrated into solar cells with full-area passivating contacts, such as polysilicon or silicon heterojunction. Augmenting the superior electrical performance of passivating contacts with the additional optical-thermal benefit from an optimized sub-bandgap reflector could further enhance their applicability in the PV module market.

Acknowledgment

The views expressed in this article do not necessarily represent the views of the U.S. Department of Energy or the U.S. Government. The U.S. Government retains and the publisher, by accepting the article for publication, acknowledges that the U.S. Government retains a nonexclusive, paid-up, irrevocable, worldwide license to publish or reproduce the published form of this work, or allow others to do so, for U.S. Government purposes. The authors would like to thank Rafell Williams and Tao Song for EQE measurements, Paul Ndione, Steve Rummel, and Allan Anderberg for temperature-dependent laboratory *I–V* measurements, Byron McDanold for module fabrication, and Derek Holsapple for reflectance measurements.

References

[1] R. Dubey *et al.*, "Performance degradation in field-aged crystalline silicon PV modules in different Indian climatic conditions," in *Proc. 40th IEEE Photovolt. Specialists Conf.*, 2014, pp. 3182–3187.

[2] J. Y. Ye, T. Reindl, A. G. Aberle, and T. M. Walsh, "Performance degradation of various PV module technologies in tropical Singapore," *IEEE J. Photovolt.*, vol. 4, no. 5, pp. 1288–1294, Sep. 2014.

[3] I. Haedrich, D. C. Jordan, and M. Ernst, "Methodology to predict annual yield losses and gains caused by solar module design and materials under field exposure," *Sol. Energy Mater. Sol. Cells*, vol. 202, Nov. 2019, Art. no. 110069.

[4] N. Strevel, L. Trippel, and M. Gloeckler, "Performance characterization and superior energy yield of first solar PV power plants in high-temperature conditions," *Photovolt. Int.*, vol. 17, pp. 148–154, 2012.

[5] P. Singh and N. Ravindra, "Temperature dependence of solar cell performance—An analysis," *Sol. Energy Mater. Sol. Cells*, vol. 101, pp. 36–45, 2012.

[6] J. Haschke *et al.*, "The impact of silicon solar cell architecture and cell interconnection on energy yield in hot & sunny climates," *Energy Environ. Sci.*, vol. 10, no. 5, pp. 1196–1206, 2017.

[7] A. Ndiaye *et al.*, "Degradations of silicon photovoltaic modules: A literature review," *Sol. Energy*, vol. 96, pp. 140–151, Oct. 2013.

[8] H. Gopalakrishna, A. Sinha, K. Dolia, D. Jordan, and G. Tamizhmani, "Nondestructive characterization and accelerated UV testing of browned field-aged PV modules," *IEEE J. Photovolt.*, vol. 9, no. 6, pp. 1733–1740, Nov. 2019.

[9] S. Kurtz *et al.*, "Evaluation of high-temperature exposure of photovoltaic modules," *Prog. Photovolt., Res. Appl.*, vol. 19, pp. 954–965, 2011.

[10] A. Anand, A. Shukla, H. Panchal, and A. Sharma, "Thermal regulation of photovoltaic system for enhanced power production: A review," *J. Energy Storage*, vol. 35, Mar. 2021, Art. no. 102236.

[11] O. Dupré, R. Vaillon, and M. A. Green, "A full thermal model for photovoltaic devices," *Sol. Energy*, vol. 140, pp. 73–82, Dec. 2016.

[12] L. C. Andreani, A. Bozzola, P. Kowalczewski, M. Liscidini, and L. Redorici, "Silicon solar cells: Toward the efficiency limits," *Adv. Phys. X*, vol. 4, no. 1, 2019, Art. no. 1548305.

[13] I. M. Slauch, M. G. Deceglie, T. J. Silverman, and V. E. Ferry, "Spectrally selective mirrors with combined optical and thermal benefit for photovoltaic module thermal management," *ACS Photon.*, vol. 5, no. 4, pp. 1528–1538, Mar. 2018.

[14] T. J. Silverman *et al.*, "Reducing operating temperature in photovoltaic modules," *IEEE J. Photovolt.*, vol. 8, no. 2, pp. 532–540, Mar. 2018.

[15] R. Vaillon, O. Dupré, R. B. Cal, and M. Calaf, "Pathways for mitigating thermal losses in solar photovoltaics," *Sci. Rep.*, vol. 8, no. 1, 2018, Art. no. 13163.

[16] G. Perrakis *et al.*, "Passive radiative cooling and other photonic approaches for the temperature control of photovoltaics: A comparative study for crystalline silicon-based architectures," *Opt. Exp.*, vol. 28, no. 13, pp. 18548–18565, 2020.

[17] I. M. Slauch, M. G. Deceglie, T. J. Silverman, and V. E. Ferry, "Spectrally selective mirrors with combined optical and thermal benefit for photovoltaic module thermal management," *ACS Photon.*, vol. 5, no. 4, pp. 1528–1538, 2018.

[18] I. M. Slauch, M. G. Deceglie, T. J. Silverman, and V. E. Ferry, "Model for characterization and optimization of spectrally selective structures to reduce the operating temperature and improve the energy yield of photovoltaic modules," *ACS Appl. Energy Mater.*, vol. 2, no. 5, pp. 3614–3623, 2019.

[19] I. M. Slauch, M. G. Deceglie, T. J. Silverman, and V. E. Ferry, "Two-layer anti-reflection coatings with optimized sub-bandgap reflection for solar modules," in *Proc. SPIE*, 2018, pp. 133–140.

[20] I. M. Slauch, M. G. Deceglie, T. J. Silverman, and V. E. Ferry, "Optical approaches for passive thermal management in c-Si photovoltaic modules," *Cell Rep. Phys. Sci.*, vol. 2, no. 5, 2021, Art. no. 100430.

[21] Z. C. Holman, A. Descoeudres, S. De Wolf, and C. Ballif, "Record infrared internal quantum efficiency in silicon heterojunction solar cells with dielectric/metal rear reflectors," *IEEE J. Photovolt.*, vol. 3, no. 4, pp. 1243–1249, Oct. 2013.

[22] Z. C. Holman, S. De Wolf, and C. Ballif, "Improving metal reflectors by suppressing surface plasmon polaritons: A priori calculation of the internal reflectance of a solar cell," *Light, Sci. Appl.*, vol. 2, no. 10, 2013, Art. no. e106.

[23] Z. C. Holman *et al.*, "Parasitic absorption in the rear reflector of a silicon solar cell: Simulation and measurement of the sub-bandgap reflectance for common dielectric/metal reflectors," *Sol. Energy Mater. Sol. Cells*, vol. 120, pp. 426–430, Jan. 2014.

[24] I. Subedi, T. J. Silverman, M. G. Deceglie, and N. J. Podraza, "Al+ Si interface optical properties obtained in the Si solar cell configuration," *Phys. Status Solidi A, Appl. Mater. Sci.*, vol. 214, no. 12, 2017, Art. no. 1700480.

[25] I. Subedi, T. J. Silverman, M. G. Deceglie, and N. J. Podraza, "PERC silicon PV infrared to ultraviolet optical model," *Sol. Energy Mater. Sol. Cells*, vol. 215, Sep. 2020, Art. no. 110655.

[26] M. R. Vogt *et al.*, "Reduced module operating temperature and increased yield of modules with PERC instead of Al-BSF solar cells," *IEEE J. Photovolt.*, vol. 7, no. 1, pp. 44–50, Jan. 2017.

[27] J. L. Bryan *et al.*, "Inserting a low-refractive-index dielectric rear reflector into PERC cells: Challenges and opportunities," in *Proc. 46th IEEE Photovolt. Specialists Conf.*, 2019, pp. 0648–0652.

[28] J. L. Bryan, T. J. Silverman, M. G. Deceglie, and Z. C. Holman, "Thermal model to quantify the impact of sub-bandgap reflectance on operating temperature of fielded PV modules," *Sol. Energy*, vol. 220, pp. 246–250, May 2021.

[29] P. Firth and Z. C. Holman, "Aerosol impaction-driven assembly system for the production of uniform nanoparticle thin films with independently tunable thickness and porosity," *ACS Appl. Nano Mater.*, vol. 1, no. 8, pp. 4351–4357, 2018.

[30] M. Boccard *et al.*, "Low-refractive-index nanoparticle interlayers to reduce parasitic absorption in metallic rear reflectors of solar cells," *Phys. Status Solidi (a)*, vol. 214, no. 10, 2017, Art. no. 1700179.

[31] K. Emery, D. Dunlavy, H. Field, and T. Moriarty, "Photovoltaic spectral responsivity measurements," National Renewable Energy Lab., Golden, CO, USA, Rep. NREL/CP-530-23878, Jul. 1998.

[32] B. Marion, S. Rummel, and A. Anderberg, "Current–voltage curve translation by bilinear interpolation," *Prog. Photovolt., Res. Appl.*, vol. 12, no. 8, pp. 593–607, Nov. 2004.

[33] Y. Tsuno, Y. Hishikawa, and K. Kurokawa, "Modeling of the I–V curves of the PV modules using linear interpolation/extrapolation," *Sol. Energy Mater. Sol. Cells*, vol. 93, no. 6/7, pp. 1070–1073, Jun. 2009.

[34] J. Palyvos, "A survey of wind convection coefficient correlations for building envelope energy systems' modeling," *Appl. Thermal Eng.*, vol. 28, no. 8/9, pp. 801–808, 2008.

[35] H. Schulte-Huxel, T. J. Silverman, M. G. Deceglie, D. J. Friedman, and A. C. Tamboli, "Energy yield analysis of multiterminal Si-based tandem solar cells," *IEEE J. Photovolt.*, vol. 8, no. 5, pp. 1376–1383, Jul. 2018.

[36] S. K. Chunduri and M. Schmela, "Market survey metallization pastes 2019/20," TaiyangNews, Duesseldorf, Germany, Mar. 2020. [Online]. Available: http://taiyangnews.info/reports/market-survey-metallization-pastes-201920/

[37] P. Padhamnath *et al.*, "Development of thin polysilicon layers for application in monoPoly$^{\mathrm{TM}}$ cells with screen-printed and fired metallization," *Sol. Energy Mater. Sol. Cells*, vol. 207, 2020, Art. no. 110358.